

REMARKS

This Amendment is submitted in response to the final Office Action mailed on November 9, 2010. A Request for Continued Examination (“RCE”) (\$810.00) is submitted herewith. The Director is authorized to charge \$810.00 for the RCE and any additional fees which may be required, or to credit any overpayment to Deposit Account No. 02-1818. If such a withdrawal is made, please indicate the Attorney Docket No. 3712174-00491 on the account statement.

Claims 41, 44-45, 47-63, 66-67 and 69-88 are pending in this application. Claims 50-62 and 72-80 were previously withdrawn from consideration, and Claims 1-40, 42-43, 46, 64-65 and 68 were previously canceled without prejudice or disclaimer. In the Office Action, Claims 41, 44-45, 47-49, 63, 66-67, 69-71 and 81-88 are rejected under 35 U.S.C. §103. Claims 41, 49, 63 and 71 are further rejected for nonstatutory double patenting. In response, Claims 41 and 63 have been amended. The amendments do not add new matter. At least in view of the amendments and/or for the reasons set forth below, Applicants respectfully submit that the rejections should be withdrawn.

In the Office Action, Claims 41, 49, 63, 71, 81-82, 84-85 and 87-88 are rejected under 35 U.S.C. §103(a) as being unpatentable over U.S. Patent No. 6,203,944 B1 to Turner et al. (“*Turner*”). In response, Applicants have amended Claims 41 and 63. In view of the amendments and/or for at least the reasons set forth below, Applicants respectfully submit that *Turner* fails to disclose each and every element of independent Claims 41 and 63 and Claims 49, 71, 81-82, 84-85 and 87-88 that depend therefrom.

Currently amended independent Claims 41 and 63 recite, in part, an anode material having a reaction phase containing: an element selected from the group consisting of silicon and tin; carbon; and at least one constituent selected from the group consisting of nickel, copper, iron, cobalt, manganese, zinc, indium, and silver, wherein a ratio of carbon in the reaction phase ranges from about 10% by weight to about 40% by weight, and wherein a peak of carbon is obtained in a region lower than about 284.5 eV by X-ray photoelectron spectroscopy, and the carbon in the reaction phase exists among the tin and is bonded to form a carbide with a metal element or metalloid element contained in the reaction phase such that the electric charge density of the carbon in the reaction phase is increased by interaction with the metal element or metalloid element. The amendments do not add new matter. The amendments are supported in the Specification at, for example, page 2, paragraphs 28-29; Table 1-7, Examples 1-38 and 1-39. In contrast, *Turner* fails to disclose every element of Claims 41 and 63.

For example, *Turner* fails to disclose or suggest an anode material having a reaction phase containing carbon as required, in part, by independent Claims 41 and 63. The Patent Office asserts that *Turner* teaches an anode material having a reaction phase containing tin, iron and graphite. See, Office Action, page 4, lines 20-23; page 5, lines 1-3. However, the portion of *Turner* relied on by the Patent Office merely discloses an anode mixture having two phases: a Sn₂Fe phase and a SnFe₃C phase. See, *Turner*, column 19, lines 61-63 (Example 17); column 20, lines 31-33 (Example 19). Nowhere does *Turner* teach or suggest that the SnFe₃C phase is the reaction phase. Instead, *Turner* merely teaches that the Sn₂Fe phase reacts with lithium during cycling. See, *Turner*, column 18, lines 9-10.

In response to Applicants' previous arguments regarding this point, the Patent Office asserted that "there is no teaching in *Turner* that the SnFe₃C phase is a non-reactive phase containing carbon. Since *Turner* et al discloses an anode material comprising the same elements. . . formed by the same process as the present invention, the examiner maintains the contention that the SnFe₃C phase is a reaction phase." See, Office Action dated May 20, 2010, page 10, lines 12-16. In response, Applicants respectfully note that one of ordinary skill in the art would understand that the SnFe₃C phase of a mixture containing Sn₂Fe and SnFe₃C phases is inactive. For example, an article co-written by the inventors of *Turner* expressly teaches that when mechanical alloying is used to form composite mixtures of Sn₂Fe and SnFe₃C phases (as in *Turner*), the SnFe₃C phase is inactive and "do[es] not alloy with lithium." See, "Structure and properties of sequentially sputtered molybdenum-tin films" by J.R. Dahn et al., Thin Films 408 (2002): 111-122 (emphasis added), p. 111, attached hereto as Exhibit A; *Kohno*, column 2, lines 9-13 (stating that the SnFe₃C phase of a Sn₂Fe/SnFe₃C mixed phase composition "does not absorb Li"). Thus, *Turner* fails to disclose a reaction phase containing carbon.

Applicants further note that one of ordinary skill in the art would understand that the anode material of *Turner* is not necessarily formed by the same process as the claimed composition. For example, the present Specification teaches preparing its anode material by mixing graphite with powders in which other components are alloyed as a raw material for elements other than carbon in a total amount of 1 kg (i.e., 1000 g) using about 18 kg of hard chromium balls having a diameter of 9 mm. See, Specification, page 6, paragraph 77. The Specification further discloses that the agitation device is operated for 10 hours at a speed of 250 rpm, then stopped for 10 minutes and repeated until the total operation time is 20 hours. See, Specification, page 6, paragraph 77.

In contrast, *Turner* merely teaches preparing its powder by adding iron, tin and graphite in a total amount of approximately 2 g directly to a ball milling vial having two steel balls of 12.7 mm diameter and milling the sample for 20 hours. See, *Turner*, column 17, lines 27-41 (Example 8); column 19, lines 55-60 (Example 17); column 20, lines 25-30 (Example 19). Nowhere does *Turner* teach or suggest the mixing speed of its sample, nor that its mixing is stopped for 10 minutes after 10 hours of operation. Furthermore, the amount of material mixed is much less than that of the present Specification, and the diameter and type of mixing balls are also distinguishable from those used in the present Specification. As such, one of ordinary skill in the art would understand that the samples of *Turner* are not necessarily the same as the claimed anode material.

Accordingly, Applicants respectfully request that the rejection of Claims 41, 49, 63, 71, 81-82, 84-85 and 87-88 under 35 U.S.C. §103(a) to *Turner* be withdrawn.

In the Office Action, Claims 41, 45, 47-49, 63, 67, 69-71, 81-82, 84-85 and 87-88 are rejected under 35 U.S.C. §103(a) as being unpatentable over U.S. Patent No. 6,495,291 B1 to Kohno et al. ("Kohno") in view of Japanese Patent Publication No. 2000-311681 A to Kawakami et al. ("Kawakami"). In response, Applicants have amended Claims 41 and 63. In view of the amendments and/or for at least the reasons set forth below, Applicants respectfully submit that, even if combinable, the cited references fail to disclose every element of independent Claims 41 and 63 and Claims 45, 47-49, 67, 69-71, 81-82, 84-85 and 87-88 that depend therefrom.

For example, even if combinable, *Kohno* and *Kawakami* fail to disclose or suggest an anode material having a reaction phase containing at least one constituent selected from the group consisting of nickel, copper, iron, cobalt, manganese, zinc, indium, and silver as recited, in part, by independent Claims 41 and 63. The Patent Office asserts that *Kohno* discloses a "negative electrode active material" having a "composition" that is $M1_xM2_yC_{1-x-y}$ where M1 is Si, Ge, Sn, Pb, B, Al, Ga, In, Sb or Zn and M2 is Mg, Ca, Sr, Ba, Ti, Zr, V, Ta, Cr, Mo or W. See, Office Action, page 7, lines 1-10. The Patent Office further asserts that *Kawakami* teaches negative electrode material particles having a composition Sn-A-X where A is a transition metal such as Mn, Fe, Co, Ni, Cu or Ag and X is may be carbon. See, Office Action, page 7, lines 14-20; page 8, lines 1-2. The Patent Office then asserts that it would have been obvious to substitute the M2 element of *Kohno* with Ni, Cu, Fe, Co, Mn, Zn, In or Ag in order to obtain a battery having a long cycle life, high capacity and high energy density. See, Office Action, page 8, lines 3-9.

Kohno discloses a composite material having a carbon-containing phase and a crystal phase containing the elements M1 and M2. See, *Kohno*, column 5, lines 59-63; column 6, lines 54-59. Although *Kohno* discloses that the carbon-containing phase may contain the elements or atoms constituting the crystal phase in addition to carbon, nowhere does *Kohno* teach or suggest a single phase containing carbon, silicon or tin (i.e., M1), and an element selected from the group consisting of nickel, copper, iron, cobalt, manganese, zinc, indium, and silver. See, *Kohno*, column 7, lines 6-12. In fact, the Patent Office admits that *Kohno* fails to disclose including nickel, copper, iron, cobalt, manganese, zinc, indium or silver in its reaction phase and instead relies on *Kawakami* for the claimed element. See, Office Action, page 7, lines 14-16.

However, *Kawakami* merely describes negative electrode material particles having a composition Sn-A-X where X may be carbon and A is a transition metal such as Mn, Fe, Co, Ni, Cu or Ag. See, *Kawakami*, paragraphs 26-27 and 33. As explained in the present Specification, the reaction phase of an anode material, as opposed to the overall composition of the material, can be identified by comparing X-ray diffraction charts before and after electrochemical reaction and identifying the diffraction peak which changes after electrochemical reaction. See, Specification, page 2, paragraph 33. Yet nowhere does *Kawakami* identify its “reaction phase” or suggest that the transition metal A is included in a reaction phase of its material. As such, even if combinable, *Kohno* and *Kawakami* fail to disclose an anode material having a reaction phase containing at least one constituent selected from the group consisting of nickel, copper, iron, cobalt, manganese, zinc, indium, and silver as required, in part, by the present claims.

Moreover, even if combinable, *Kohno* and *Kawakami* fail to disclose or suggest an anode material wherein a ratio of carbon in the reaction phase ranges from about 10% by weight to about 40% by weight as recited, in part, by Claims 41 and 63. The Patent Office asserts that *Kohno* describes an example of its negative electrode material, $Sn_{0.25}Mg_{0.03}C_{0.72}$, in which the amount of carbon corresponds to 22.1 wt %. See, Office Action, page 7, lines 9-13. However, as discussed previously, the composition of the reaction phase is not necessarily the same as the overall material composition. In fact, *Kohno* expressly teaches that its material includes carbon and crystalline phases. See, *Kohno*, column 5, lines 59-63; column 6, lines 54-59. Yet nowhere does *Kohno* disclose or even suggest the specific distribution of carbon, M1 and M2 elements among the phases, nor that the amount of carbon in one of the phases is between 10 and 40 wt %. As such, even if combinable, *Kohno* and *Kawakami* fail to suggest an anode material wherein a ratio of carbon in the reaction phase ranges from about 10% by weight to about 40% by weight.

Accordingly, Applicants respectfully request that the rejection of Claims 41, 45, 47-49, 63, 67, 69-71, 81-82, 84-85 and 87-88 under 35 U.S.C. §103(a) to *Kohno* and *Kawakami* be withdrawn.

In the Office Action, Claims 44 and 66 are rejected under 35 U.S.C. §103(a) as being unpatentable over *Kohno* in view of *Kawakami*. For at least the reasons set forth below, Applicants respectfully submit that, even if combinable, the cited references fail to disclose or suggest each and every element of Claims 44 and 66.

As discussed previously, the combination of *Kohno* and *Kawakami* fails to disclose or suggest an anode material: (1) having a reaction phase containing at least one constituent selected from the group consisting of nickel, copper, iron, cobalt, manganese, zinc, indium, and silver; and (2) wherein a ratio of carbon in the reaction phase ranges from about 10% by weight to about 40% by weight as required, in part, by independent Claims 41 and 63 from which Claims 44 and 66 depend. The Patent Office further asserts that it would have been obvious to try to form an alloy using a constituent selected from the group consisting of zinc, indium and silver. See, Office Action, page 10, lines 11-14. However, even if one of ordinary skill in the art were to use zinc, indium or silver in the composition of *Kohno* or *Kawakami*, the cited references fail to teach that such an element is contained in a reaction phase with carbon or that the amount of carbon in the reaction phase is between about 10% and about 40% by weight. Thus, Applicants respectfully submit that, even if combinable, *Kohno* and *Kawakami* fail to disclose every element of Claims 44 and 66.

Accordingly, Applicants respectfully request that the rejection of Claims 44 and 66 under 35 U.S.C. §103(a) to *Kohno* and *Kawakami* be withdrawn.

In the Office Action, Claims 83 and 86 are rejected under 35 U.S.C. §103(a) as being unpatentable over *Kohno* in view of *Kawakami*. For at least the reasons set forth below, Applicants respectfully submit that, even if combinable, the cited references fail to disclose or suggest each and every element of Claims 83 and 86.

As discussed previously, the combination of *Kohno* and *Kawakami* fails to disclose or suggest an anode material: (1) having a reaction phase containing at least one constituent selected from the group consisting of nickel, copper, iron, cobalt, manganese, zinc, indium, and silver; and (2) wherein a ratio of carbon in the reaction phase ranges from about 10% by weight to about 40% by weight as required, in part, by independent Claims 41 and 63 from which Claims 44 and 66 depend. The Patent Office further asserts that it would have been obvious to

include a carbonaceous material capable of inserting and extracting lithium in an equal ratio to the anode material. See, Office Action, page 10, lines 21-22; page 11, lines 1-5. However, this assertion fails to remedy the deficiencies of *Kohno* and *Kawakami* with respect to Claims 83 and 86.

Accordingly, Applicants respectfully request that the rejection of Claims 83 and 896 under 35 U.S.C. §103(a) to *Kohno* and *Kawakami* be withdrawn.

In the Office Action, Claim 63 is provisionally rejected under the judicially created doctrine of obviousness-type double patenting over Claims 10 and 16 of U.S. Patent Application No. 11/267,641. Applicants respectfully note that this rejection is provisional and, thus, Applicants will address this rejection at such time as allowability has been indicated in one of the cases, if the rejection is still relevant at such time.

In the Office Action, Claims 41 and 63 are provisionally rejected under the judicially created doctrine of obviousness-type double patenting over Claims 1-3, 9-11, 18-19 and 26-27 of U.S. Patent Application No. 12/026,594. Applicants respectfully note that this rejection is provisional and, thus, Applicants will address this rejection at such time as allowability has been indicated in one of the cases, if the rejection is still relevant at such time.

In the Office Action, Claims 41, 49, 63 and 71 are provisionally rejected under the judicially created doctrine of obviousness-type double patenting over Claims 1-2 and 7-8 of U.S. Patent Application No. 11/268,010. Applicants respectfully note that this rejection is provisional and, thus, Applicants will address this rejection at such time as allowability has been indicated in one of the cases, if the rejection is still relevant at such time.

In the Office Action, Claims 41 and 63 are provisionally rejected under the judicially created doctrine of obviousness-type double patenting over Claims 1-3 and 10-12 of U.S. Patent Application No. 11/225,540. In response, Applicants respectfully submit that Claims 1-3 and 10-12 are patentably distinct from Claims 41-42 and 63-64 of the present application because Claims 1-3 and 10-12 require a CoSnC containing material, whereas Claims 41 and 63 merely require a reaction phase containing tin and at least one constituent selected from the group consisting of nickel, copper, iron, cobalt, manganese, zinc, indium, and silver. Moreover, Applicants respectfully note that this rejection is provisional and, thus, Applicants will further address this rejection at such time as allowability has been indicated in one of the cases, if the rejection is still relevant at such time.

Accordingly, Applicants respectfully request that the provisional rejections of Claims 41, 49, 63 and 71 under obviousness-type double patenting be withdrawn.

For the foregoing reasons, Applicants respectfully submit that the present application is in condition for allowance and earnestly solicit reconsideration of same.

Respectfully submitted,

K&L GATES LLP

BY


Thomas C. Basso
Reg. No. 46,541
Customer No. 29175

Date: February 9, 2011

Structure and properties of sequentially sputtered molybdenum–tin films

J.R. Dahn^{a,*}, R.L. Turner^b, Ou Mao^a, R.A. Dunlap^a, A.E. George^a, M.M. Buckett^b, D.J. McClure^b, L.J. Krause^b

^aDepartments of Physics and Chemistry, Dalhousie University, Halifax, NS, Canada B3H 3J5

^b3M Co., 3M Center, St. Paul, MN, 55144-1000, USA

Received 4 September 2001; received in revised form 19 January 2002; accepted 20 February 2002

Abstract

Rotating a water-cooled substrate rapidly under Mo and Sn sputter sources made sequentially sputtered molybdenum–tin thin films. The layer thickness deposited during each circuit under each source was selected between 2 and 20 Å and films of several micrometers overall thickness were prepared. The produced films were characterized using wide-angle and small-angle X-ray scattering, ^{119}Sn Mössbauer spectroscopy, differential scanning calorimetry and transmission electron microscopy. Films of three major types are observed: (1) homogeneous crystalline body centered cubic $\text{Mo}_{1-x}\text{Sn}_x$ is produced when x is less than approximately 0.45 and when the layer thickness deposited in each pass under the targets is small; (2) nanocrystalline BCC $\text{Mo}_{1-x}\text{Sn}_x$ having x approximately equal to 0.45 coexisting with nanocrystalline tin when the overall tin content is greater than 45% atomic and the layer thickness deposited in each pass under the targets is small; and (3) lamina of composition modulated $\text{Mo}_{1-x}\text{Sn}_x$ disturbed by nanoscopic clusters of tin when the overall tin content is greater than approximately 40% atomic and the layer thickness of Mo deposited in each pass is greater than approximately 6 Å. This is the first report of BCC $\text{Mo}_{1-x}\text{Sn}_x$ for $0 \leq x \leq 0.45$. A ‘phase diagram’ of the observed film types is presented. © 2002 Elsevier Science B.V. All rights reserved.

Keywords: Molybdenum; Multilayers; Tin

1. Introduction

Sputter deposition has been used for many years to prepare novel multi-component structures [1–3]. As an example, artificial metallic superlattices [4] containing many layers of two metals deposited sequentially have been extensively studied. The diffusion rates of the freshly deposited species perpendicular to the layers governs the interface sharpness, while rapid diffusion of one or both species along the surface can create mixtures of nanometer or micrometer-sized grains of different phases and completely disturb the superlattice structure. By careful selection of the pair of elements, the layer thickness deposited during each pass under the sputter targets, substrate temperature, etc., it is possible to prepare a wide variety of film structures ranging from amorphous mixtures to well ordered superlattices. For this reason, we selected sequential sputter deposition in

our attempts to prepare nanocomposites for lithium-ion battery electrode applications.

Metals that alloy with lithium have been studied as anodes for Li batteries for many years. However, although elements like tin have large capacity for lithium, particles of the alloys crack and fragment during the repeated alloying and de-alloying which occurs as cells are charged and discharged [5]. The research groups of Huggins and Boukamp [6] and Yang et al. [7] have proposed that alloy fragmentation can be reduced if grain of the active alloying species are embedded in a ‘matrix’ which holds them together. We recently improved on their ideas by preparing nanocomposites of particles consisting of nanoscopic grains of active Sn_2Fe (alloys with lithium) and inactive SnFe_3C (do not alloy with lithium) phases [8,9]. Mechanical alloying was used to prepare the $\text{Sn}_2\text{Fe}/\text{SnFe}_3\text{C}$ active/inactive nanocomposites. Provided that the size of the active grains is only a few nanometers, the discreet Li–Sn phases in the bulk Li–Sn phase diagram [10] apparently do not form and homogeneous expansion of

*Corresponding author. Tel.: +1-902-494-2312; fax: +1-902-494-5191.

E-mail address: jeff.dahn@dal.ca (J.R. Dahn).

the active grains occurs as Li alloys with the material. Cracking and fragmentation is prevented and good performance is observed.

It was our opinion that sequential sputter deposition of tin and a second element would give better control over the types of nanostructures that could be prepared. As a first trial, we picked molybdenum as the second element. The molybdenum–tin phase diagram has not been properly mapped; in fact only a provisional phase diagram [10,11] exists. The line phases Mo_3Sn and MoSn_2 are claimed to exist, as well as a possible phase of broad homogeneity designated as MoSn . Much of the confusion stems from numerous reports stating no reaction between Mo and liquid tin. However, on page 41 of Brewer [11], Brewer states that Brown [12] prepared the Mo–Sn phases by heating the Mo and Sn in a shaking device which abraded a protective layer off the Mo, allowing reactions to proceed. Killpatrick [13] also agrees that Mo_3Sn exists and is a body centered cubic alloy at room temperature with lattice constant $a = 3.165 \text{ \AA}$. Thus, we were hopeful that some type of active (Sn-rich)/inactive (Mo-rich) nanocomposite could be prepared by appropriate selection of sequential sputter deposition conditions.

Tin has a low melting point (232°C) and Mo has a very high one (2617°C). Hence, one expects the diffusion rates of the tin atoms immediately after deposition on a room temperature substrate to be much larger than that of the Mo atoms. The fact that Mo–Sn intermetallic compounds exist, suggests that in equilibrium Sn should diffuse into the Mo layers to make homogeneous phases. However, if the diffusion rate of tin parallel to the substrate is larger than the diffusion rate perpendicular (into the Mo) to the substrate, and if relatively thick layers of Sn and Mo are deposited, nanoscopic clusters of tin could form as the tin diffuses parallel to the substrate after each rotation under the tin target. The tin clusters would be ‘buried’ under subsequent Mo layers. We felt that this could create a very desirable nanostructure for Li battery applications.

Here, we describe the preparation and characterization of sequentially sputtered Mo–Sn films. The major goal of this work is to understand how the nanostructure of the films depends on the deposition conditions. The electrochemical properties of these films are described elsewhere [14].

2. Experimental

Thin films were prepared by sequential sputtering using a modified Perkin-Elmer Randex Model 2400-8SA sputtering system. Commercially available 150-mm diameter DC magnetron sputtering sources of Mo and Sn were obtained from Materials Science (San Diego, CA, USA). The sputtering sources were powered by Advanced Energy Model MDX-10 DC sputtering power

supplies operating in constant current mode. The turntable drive unit of the Randex system was replaced with a stepper motor to improve rotation speed range and control. The system was pumped with a diffusion pump backed by a conventional rotary vane pump.

Sputtering was performed at argon pressures in the range of 3–30 mtorr. The pressure was maintained by controlling the argon flow in combination with a venetian blind-style conductance limiter placed over the diffusion pump.

A ‘donut shaped’ copper foil of $25\text{-}\mu\text{m}$ thickness was bonded to the water cooled substrate turntable of the Randex system using double sided adhesive tape (3M brand Y9415). The system was closed and pumped down to base pressures less than 10^{-5} torr. The copper substrates were typically etched for a period of 30 min to ensure good adhesion of the sputtered film to the copper substrate.

Following etching, the sputtering sources were started using a mechanical shutter between the sources and the substrate. This removed contaminants from the source surface without depositing them on the substrate surface. Next, a pre-layer of Mo approximately $200\text{-}\text{\AA}$ thickness was deposited to ensure good adhesion of the film to the copper substrate. Then, both sources were started at predetermined current levels and deposition initiated while the substrate was rotated at 38 rev./min. Depositions generally proceeded until films were several micrometers thick. Some specimens had a post-layer of pure tin applied after the sequential deposition was completed, to improve their electrochemical performance as is described in [14]. Table 1 lists the specimens made.

The deposition rates corresponding to particular sputtering currents were determined from a series of calibration experiments in which a single source was operated at a fixed current for a fixed period of time. The thickness of the resulting sample was measured using a profilometer. The thickness of the layer deposited during each pass under a target was then calculated from the average deposition rate in $\text{\AA}/\text{min}$ for the rotating substrate (typically between 60 and $800\text{ \AA}/\text{min}$) divided by the rotation rate. The mass deposition rates per unit sputtering current [$\text{mg}/(\text{min A})$] were calculated from the thickness deposition rates using the tabulated densities of bulk Sn and Mo. The chemical compositions of the samples were calculated assuming that the total masses of Sn and Mo in the samples were proportional to the product of the mass deposition rate per unit sputtering current, the sputtering current and the sputtering time. Atomic percentages of the elements in the samples were then calculated from the mass percentages using the atomic weights of the elements. We expect a systematic error of less than 10% in the atomic percentages quoted here.

Fig. 1 shows a schematic of the Randex system. Deposition rates were measured at positions under the center of the targets where the highest rates occur. Near the edges of the donut shaped substrates, the deposition rates were lower, by approximately a factor of 5. Thus, if 10 Å of Mo and 10 Å of Sn were deposited during each pass of the substrate under the targets in the center of the substrate, only approximately 2 Å of each would be deposited during each pass at the edges. We were careful to select samples from the center of the substrate, where the deposition rates were known, for most of the experiments described here. However, there were some instances where a comparison of the center and edge of the film, ensuring the same chemical composition, allowed improved understanding of the film growth mechanisms.

Specimens for X-ray diffraction analysis were prepared by mounting 25×50-mm sections of the films on microscope slides with double-sided tape. The samples were then pressed flat with a second microscope slide. These were placed in special slide holder which ensured the top surface of the film was on the axis of the X-ray goniometer. A Siemens D-5000 diffractometer operating in Bragg–Brentano geometry was used. The diffractometer was equipped with a Cu target X-ray tube and a diffracted beam monochromator. For the small-angle

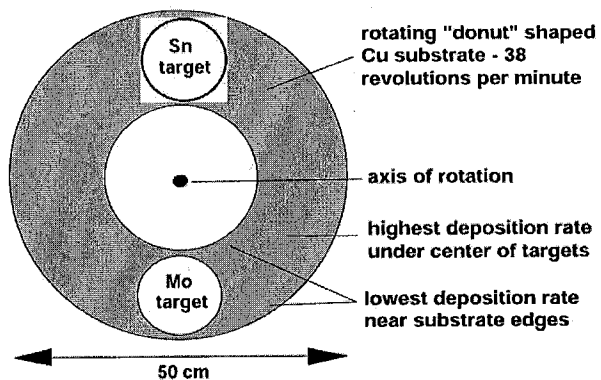


Fig. 1. Schematic diagram of the 'donut' shaped Randex target and the positions of the sputtering targets.

scans, the incident and antiscatter slits were set to 0.2° divergence so that the beam would be confined to the sample above 2° in scattering angle. Grain size estimates were made using the Scherrer equation [15].

The ^{119}Sn Mössbauer spectra were measured at room temperature using a Wissel System II constant acceleration spectrometer. Data were collected using an Ortec ACE multichannel scaling board. A $\text{Ca}^{119m}\text{SnO}_3$ source was used. The source/spectrometer had an intrinsic line

Table 1
Summary of the thick/thick Mo–Sn samples (samples 1–15), thin/thin Mo–Sn samples (samples 4 edge, 16–19) and Mo–Al sample (sample 20)

Sample	Wt.% Sn	At.% Sn	Rot. (rev./min)	Sn deposition per rev. (Å)	Mo deposition per rev. (Å)	Superlattice period (Å)	Film thickness (μm)	Mössbauer $A_1/(A_1+A_2)$ (%)	Isomer shift A_2 peak (mm/s)	Sn overlayer
1	28.8	24.6	38	5.1	9.0	None	8.1	0.0	—	No
2	44.9	39.7	38	14.6	12.8	15.2	5.6	—	—	Yes
3	44.8	39.6	38	10.2	9.0	10.4	5.3	60	2.66	No
4	44.9	39.7	38	14.9	12.8	14.5	4.4	67 center	2.38	No
4 edge	44.9	39.7	38	?	?	None	?	10 edge	—	—
5	48.6	43.3	38	14.6	11.1	4.2	61	—	2.50	No
6	48.6	43.3	38	14.6	11.1	12.6	4.9	—	—	Yes
7	50.6	45.2	38	14.6	10.2	4.3	61	—	2.68	No
8	53.7	48.3	38	14.6	9.0	11.1	5.1	61	2.73	No
9	53.7	48.3	38	14.6	9.0	8.7	59	—	2.59	No
10	53.8	48.2	38	14.6	9.0	11.3	5.3	—	—	Yes
11	59.9	54.6	38	14.6	7.0	4.0	57	—	2.80	No
12	59.9	54.6	38	14.6	7.0	10.4	n/a	—	—	Yes
13	61.8	56.6	38	20.4	9.0	12.3	5.2	60	2.65	No
14	64.2	59.1	38	14.6	5.8	8.5	4.9	—	—	Yes
15	64.2	59.1	38	14.6	5.8	4.2	59	—	2.89	No
16	47.3	42.0	38	2.9	2.3	None	3.4	30	—	No
17	50.6	45.2	38	2.9	2.0	None	3.5	56	2.53	No
18	54.5	49.1	38	2.9	1.7	None	3.4	57	2.65	No
19	58.9	53.6	38	2.9	1.5	None	3.2	58	2.74	No
20	36.4	At.% Al	38	Al deposition per rev. (Å)	9.0	25.0	6.9	—	—	Al overlayer

width 0.78 mm/s (full width at half maximum). The velocity scale was calibrated using the peak-to-peak splitting of the outer lines of Co_2MnSn (13.134 mm/s). Sn center shifts are given relative to CaSnO_3 . Many of the spectra were fitted to extract information about the local environment around the tin nuclei. Samples which had been prepared with the metallic tin overlayer were not examined by Mössbauer spectroscopy due to the expected confusion of the spectra by the metallic tin. Tin metal foil (Aesar) was used as a standard, for comparison to the spectra from the sputtered films.

Differential scanning calorimetry (DSC) measurements were made using a TA Instruments 910 DSC. Samples of the films (on the copper substrates) were folded carefully and placed directly on the sample side of the DSC. A piece of Cu foil of the same mass was folded and used as the reference. DSC measurements were made under argon at a sweep rate of 10 °C/min.

Transmission electron microscopy measurements were made using a Hitachi H9000NAR TEM operating at 300 kV. It is capable of a point-to-point resolution of approximately 2 Å and a microprobe resolution of approximately 16 Å for X-ray microanalysis. The microanalysis instrumentation consisted of a Noran Voyager III. A Gatan slow-scan charge-coupled device camera performed direct-to-digital image acquisition and quantitative length measurements.

Samples for TEM were prepared by cutting samples of the film, embedding in 3 M Scotchcast Electrical Resin #5, followed by ultramicrotoming. Slices were typically less than approximately 20 nm.

3. Results and discussion

The films made are listed in Table 1. Several strategies were employed in the experimental design. The dependence of the film properties on both Mo and Sn layer thickness was investigated. First, a series of samples was made where the thickness of tin deposited at the center of the 'donut' (see Fig. 1) during each pass under the target was kept fixed at 14.6 Å and the Mo thickness varied from 5.8 to 12.8 Å (samples 2, 4–12, 14, 15). The atomic percentage of tin in these samples varied from 39.7 to 59.1%. Then, a series of samples was made where the amount of Mo deposited during each pass was kept constant at 9.0 Å and the Sn thickness varied from 5.1 to 20.4 Å (samples 1, 3, 8–10, 13). The atomic percentage of tin in these samples varied from 24.6 to 56.6%. Samples 1–15 are called 'thick/thick' samples to designate that the amount of Mo and Sn brought to the substrate during each pass over the target corresponded to greater than approximately 6 Å. To explore the situation corresponding to excellent atomic mixing, some samples were made with very low (less than 3 Å per pass under the targets) deposition rates. Samples 16–19 will be referred to as 'thin/thin' sam-

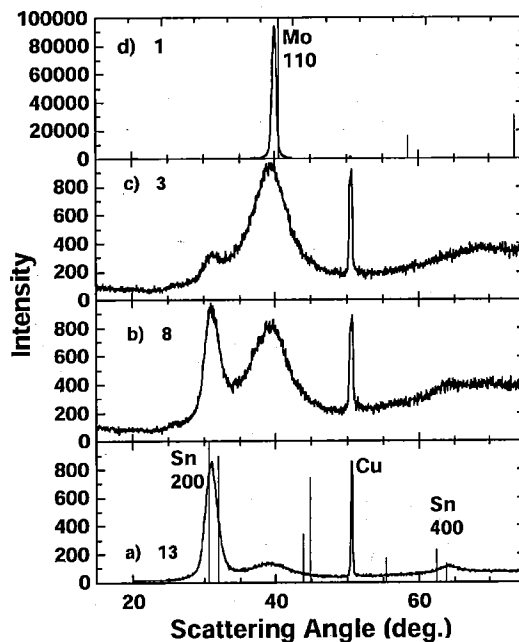


Fig. 2. X-Ray diffraction patterns for thick/thick samples. (a) Sample 13, (b) sample 8, (c) sample 3 and (d) sample 1. The positions and intensities of the Bragg peaks for white tin and b.c.c. Mo have been indicated in (a) and (d), respectively. The Cu peak is due to the substrate.

ples. The atomic percentage of tin in the thin/thin samples ranged from 42.0 to 53.6%. The center of the thin/thin samples (see Fig. 1) can be compared to the regions of the thick/thick samples at the edge of the 'donut' where deposition rates are similar. Finally, a Mo-Al film, sample 20, was prepared for comparison.

Fig. 2 shows wide angle diffraction patterns for samples 1, 3, 8 and 13, that were deposited with fixed amounts of Mo per pass under the target (9.0 Å per pass). The Sn depositions per pass were 5.1, 10.2, 14.6 and 20.4 Å, respectively. The expected peak positions and relative intensities for white tin are given in Fig. 2a and the expected peak positions and relative intensities for b.c.c. Mo are given in Fig. 2d. Sample 1 is well described by a homogeneous b.c.c. phase with a lattice constant slightly larger than that of Mo. At least 25% tin can be incorporated in a b.c.c. $\text{Mo}_{1-x}\text{Sn}_x$ phase, in agreement with literature reports of Mo_3Sn [11,13]. Sample 1 shows significant texture, that is, the 110 direction of the crystallites is predominantly normal to the substrate. Samples 3, 8 and 13 each show evidence for very small (several nm) grains of tin and of a b.c.c. phase. As the amount of tin in the samples increases the relative size of the Bragg peak due to nanocrystalline tin increases.

Fig. 3 shows small angle scattering results for samples 1, 3, 8 and 13. Sample 1 shows no evidence for superlattice periodicity, as can be expected based on it

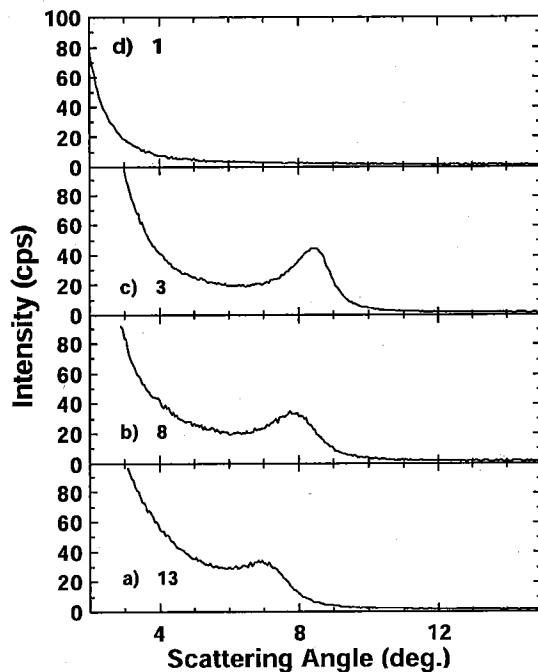


Fig. 3. Small angle X-ray scattering (counts/s under identical measuring conditions) from thick/thick samples. (a) Sample 13, (b) sample 8, (c) sample 3 and (d) sample 1.

being a homogeneous phase. Samples 3, 8 and 13 show superstructure peaks corresponding to periodicities of 10.4, 11.1 and 12.3 Å, respectively. These differ substantially from the values of 19.2, 23.6 and 29.4 Å expected if the deposited Mo and Sn layers simply deposited sequentially in a flat manner. Recall that the Mo deposition per pass under the Mo target for these samples was 9.0 Å, which is close to the superlattice periodicities observed. In addition, only one superstructure peak is observed which suggests that the superlattice extends for only a few repeats before it is interrupted by a defect.

Fig. 4 shows the wide angle diffraction patterns for samples 4, 5, 7, 11 and 15 which were made with a 14.6-Å deposition of Sn per pass under the Sn target. The Mo depositions per pass were 12.8, 11.1, 10.2, 7.0 and 5.8 Å, so that the tin content of the samples increases from sample 4 to 15. Sample 4 (Fig. 4e) has the smallest intensity for the tin peak near 31°. The intensity of the tin peak increases smoothly as the tin content increases. The halfwidths of the peaks corresponding to the tin and b.c.c. phases remain roughly constant. Fig. 5 shows the small angle scattering results for samples 14, 12, 10, 6, 2 and for the Mo-Al sample 20. The samples used here correspond closely to those shown in Fig. 4 as can be gleaned from Table 1. The superlattice periodicities of the Mo-Sn films are again approximately 2–3 Å larger than the Mo deposition per pass, and do not correspond to the sum of the Mo and

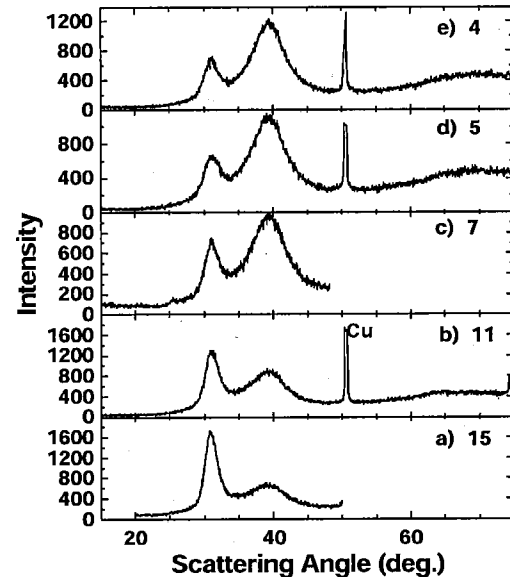


Fig. 4. X-Ray diffraction profiles for thick/thick samples. (a) Sample 15, (b) sample 11, (c) sample 7, (d) sample 5, (e) sample 4.

Sn depositions per pass. For comparison, Fig. 5a shows the diffraction pattern for a Mo-Al sequentially sputtered film where a long-ranged artificial superlattice is formed. In contrast to the data obtained for the Mo-Sn

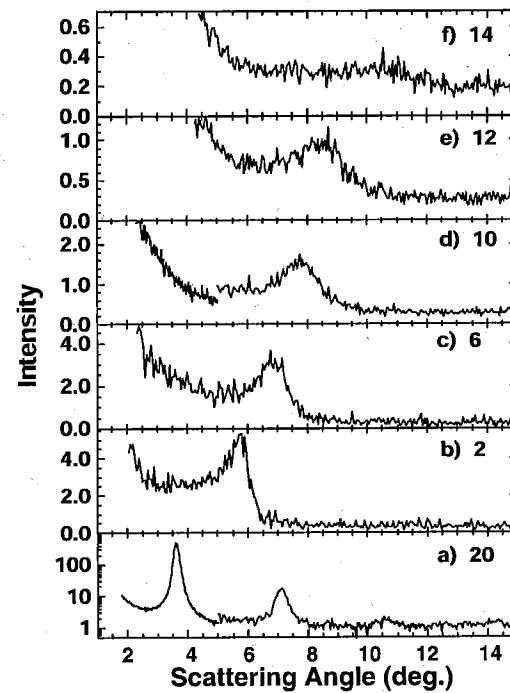


Fig. 5. Small angle X-ray scattering [counts/s under different (smaller slits) conditions from Fig. 3] for thick/thick samples. (a) Mo-Al sample 20; (b) sample 2, (c) sample 6, (d) sample 10, (e) sample 12, (f) sample 14.

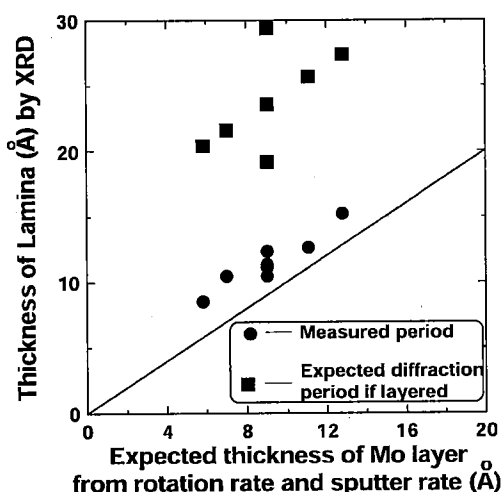


Fig. 6. Thickness of lamina as indicated by the SAX results in Figs. 3 and 5, plotted vs. the expected thickness of the Mo layer as derived from the rotation and sputter rates. Also shown is the expected period of the Mo–Sn superlattice if both Mo and Sn were deposited as perfect layers.

films, the peaks in Fig. 5a (plotted on a log scale), are narrow and four diffraction orders are observed. In this case, the observed periodicity is 25.0 Å, in good agreement with the period of 28.5 Å based on the Mo and Al depositions per pass over each target (see Table 1).

Fig. 6 shows the measured period of the superlattice and the expected period if perfect Mo and Sn layers were deposited in succession, both plotted vs. the Mo deposition thickness per pass under the target. Clearly, the superlattice period is a few angstroms larger than the Mo thickness. This means that the majority of the tin is not to be found in these lamina. After the tin layer is deposited, a small fraction of the tin (corresponding to approx. 2 or 3 Å) reacts with the Mo, or diffuses into the Mo layer. The remaining tin diffuses laterally along the surface, forming clusters of tin. The resulting proposed structure is shown in Fig. 7. There are composition modulated layers with Mo-rich cores and with Sn rich edges, coexisting with nanometer size regions of metallic tin. The superlattice structure observed in the small angle scattering experiments is due to the composition modulation, but this is frequently disturbed by the presence of the tin nanograins, hence only a single broad superstructure peak is observed. The edge of the layers should have a composition x in $\text{Mo}_{1-x}\text{Sn}_x$, equal to that of the solubility limit of Sn in the b.c.c. phase. We will determine this solubility limit later below. The peaks for the tin and b.c.c. nanograins in the wide angle X-ray patterns are broad because the size of the regions which coherently diffract X-rays are a few nanometers.

In order to confirm this structural model, transmission electron microscopy (TEM) studies were made on sam-

ple 10. The TEM analysis revealed that the microstructure contained crystalline tin particles in a compositionally modulated matrix phase. TEM analysis of samples cut from the sample along the radial direction of the 'donut' showed that the measured average tin particle size was 5 ± 1 nm by 19 ± 6 nm (approx. 30 tin particles were imaged and measured) with the long dimension parallel to the plane of the film. TEM analysis of the matrix phase showed it to be compositionally modulated perpendicular to the plane of the film, as evidenced by wandering 'stripes' in the TEM images. TEM confirms the schematic structure shown in Fig. 7.

In order to determine the composition limit of the edges of the lamina, thin/thin samples 16, 17, 18 and 19 were prepared. Fig. 8 shows their wide angle diffraction patterns. Fig. 8a shows that sample 16, $\text{Mo}_{0.58}\text{Sn}_{0.42}$ is predominantly a homogeneous b.c.c. phase. To confirm this, the substrate of sample 16 was etched away with nitric acid and the film itself recovered and gently powdered in a mortar and pestle. Fig. 9 shows the powder pattern of sample 16, clearly confirming the b.c.c. structure of this sample, and showing that the b.c.c. phase in the films displays significant preferred orientation. Fig. 8b–d shows that samples 17, 18 and 19, that contain more tin, have a much more complex structure. Samples 16 and 17 differ by only approximately 3 at.% Sn, so it is our opinion that the composition limit of the b.c.c. phase is near 42 at.% tin (subject to systematic error as discussed in Section 2).

Fig. 8d shows that sample 19 has a strong shoulder at approximately 31° as expected for extremely small (1 nm) grains of tin. This shoulder is also apparent in

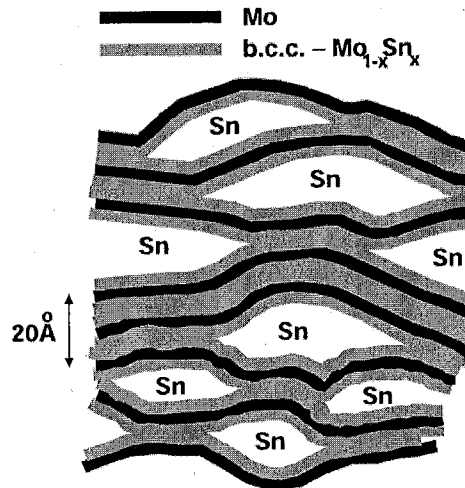


Fig. 7. Schematic of the structure of thick/thick films with tin contents greater than approximately 40%. The composition modulated layers have Mo-rich cores and edges of Sn-saturated b.c.c. $\text{Mo}_{1-x}\text{Sn}_x$. The tin nanograins are consistent with TEM and X-ray diffraction results. The scale bar gives twice the lamina thickness consistent with a 10-Å composition modulation, as observed for samples 3 and 12.

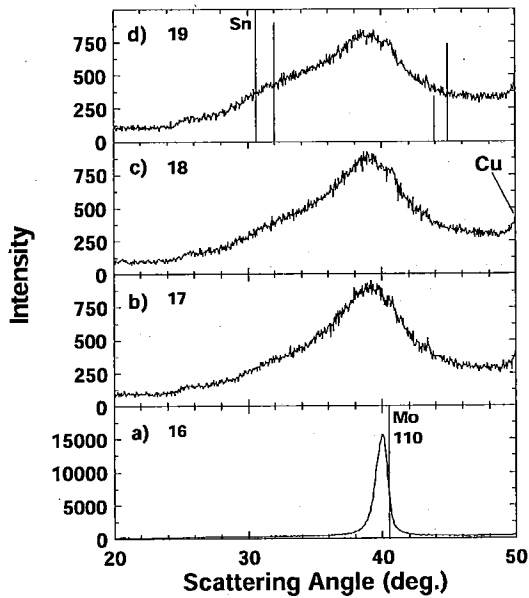


Fig. 8. X-Ray diffraction patterns observed for thin/thin samples. (a) Sample 16, (b) sample 17, (c) sample 18, (d) sample 19. The positions and intensities of the Bragg peaks from Sn and Mo are shown in (a) and (d), respectively.

samples 17 and 18, but is more difficult to observe because the tin content is smaller. It is our opinion that samples 17, 18 and 19 consist of regions of saturated b.c.c. phase (with x near 0.42 in $\text{Mo}_{1-x}\text{Sn}_x$), coexisting with nanograins of excess tin. Such a structure should show no superlattice peaks and Fig. 10 demonstrates that this is so. None of the thin/thin samples show superstructure peaks.

Fig. 11 shows a schematic of the proposed structure for the thin/thin films with x greater than 0.42 in $\text{Mo}_{1-x}\text{Sn}_x$. Since the deposition per pass is only approximately one atomic layer, intimate mixing of the Mo and Sn can take place, leading to the b.c.c. phase if the Sn content is less than approximately 0.42, or to nanoscopic regions of the b.c.c. phase at saturated composition and nanoscopic regions of tin if the Sn content is greater than approximately 0.42. If this hypothesis is true, the

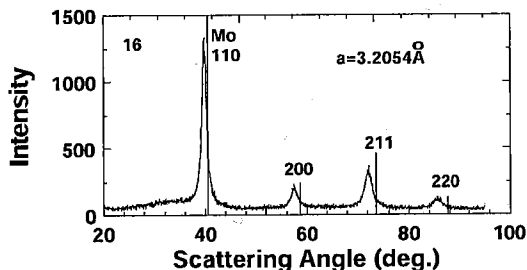


Fig. 9. X-Ray diffraction pattern of sample 16 which had been removed from the substrate and powdered. The positions and intensities of the Bragg peaks from b.c.c. Mo have been indicated.

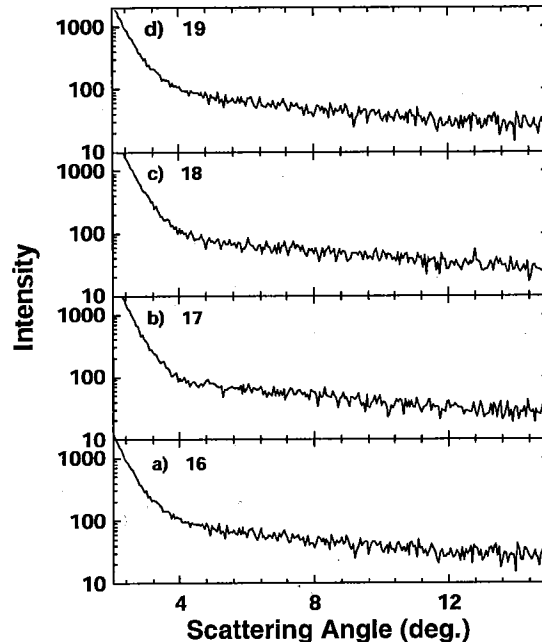


Fig. 10. Small angle scattering for thin/thin samples. (a) Sample 16, (b) sample 17, (c) sample 18, (d) sample 19.

same microstructures should be found at the edges of the thick/thick films, for tin compositions above and below 0.42.

Fig. 12a,b shows the diffraction patterns for thick/thick sample 3 taken at the center of the 'donut' and the edge of the 'donut', respectively. Sample 3 has a tin composition of approximately 0.40, less than the composition limit for the b.c.c. phase. When the deposition per pass is approximately one atomic layer, as it is at the edge of the donut, then the pure b.c.c. phase is observed. Fig. 12c shows the pattern for sample 16, for comparison. Fig. 13a,b shows the diffraction patterns for sample 13 taken at the center of the 'donut' and the edge of the 'donut' respectively. Sample 13 has a tin composition of approximately 0.57, greater than the

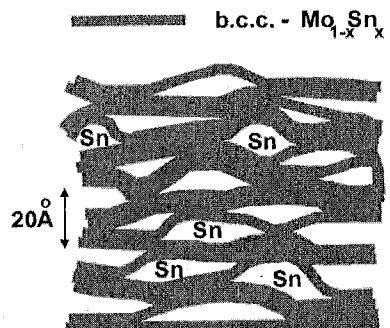


Fig. 11. Schematic of the structure of thin/thin films with x in $\text{Mo}_{1-x}\text{Sn}_x$ greater than 0.45. The scale bar is appropriate for samples 17, 18 and 19.

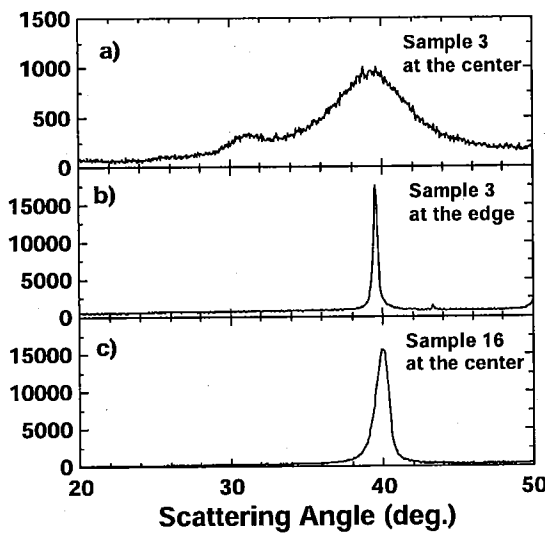


Fig. 12. Comparing the diffraction profiles of thick/thick sample 3 (x in $\text{Mo}_{1-x}\text{Sn}_x$ less than 0.45) taken at the donut center (a) and at the donut edge (b), where it is thin/thin. The diffraction pattern of thin/thin sample 16 is given in (c) for comparison.

composition limit for the b.c.c. phase. When the deposition per pass is approximately one atomic layer, as it is at the edge of the donut, a structure similar to that of thin/thin sample 19 (tin composition 0.54) is observed as shown in Fig. 12c. The edge of sample 13 shows no superlattice structure.

The b.c.c. solid solution phase for $0 < x < 0.42$ in $\text{Mo}_{1-x}\text{Sn}_x$ has not been previously reported. Of course, sputtering synthesis is a method which favors the production of metastable phases because atoms are rapidly quenched to room temperature from the plasma. Even so, it is worth reporting the cubic lattice constants of those samples which we have measured, and this is done in Fig. 14. The incorporation of Sn in $\text{Mo}_{1-x}\text{Sn}_x$ causes an increase in the cubic lattice constant.

In order to give further confirmation to the structural picture of these films presented above, Mössbauer spectra were collected on all the samples which did not have a tin overlayer. Fig. 15 shows the spectra for a collection of the thick/thick films, along with corresponding X-ray patterns. The tin content of the samples increases down the figure. Note that the edge of sample 4 is effectively a thin/thin film. The spectrum of tin metal is given in the top panel of the figure, for reference. The spectra are dominated by two absorptions, one with a center shift near 1.4 mm/s and one with a center shift near 2.6 mm/s. Due to its similarity to the center shift of metallic tin, the latter absorption is assigned to tin nuclei in nanoscopic grains of tin. Samples 1 and 4–edge predominantly only display the 1.4-mm/s absorption, which is therefore assigned to tin nuclei in the b.c.c. $\text{Mo}_{1-x}\text{Sn}_x$ phase. The other samples in Fig. 15

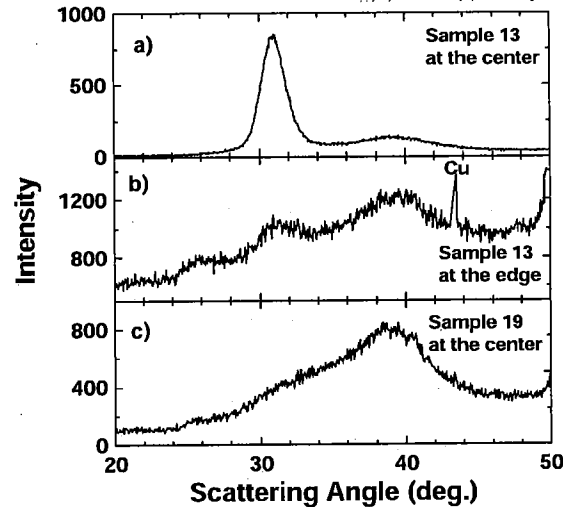


Fig. 13. Comparing the diffraction profiles of thick/thick sample 13 (x in $\text{Mo}_{1-x}\text{Sn}_x$ greater than 0.45) taken at the donut center (a) and at the donut edge (b), where it is thin/thin. The diffraction pattern of thin/thin sample 19 is given in (c) for comparison.

show evidence for both tin and b.c.c. phases from both their diffraction and Mössbauer spectra.

The Mössbauer spectra and diffraction profiles for the thin/thin samples are shown in Fig. 16. Sample 16, which is predominantly the b.c.c. phase by diffraction, shows mostly the 1.4 mm/s absorption. The other samples, show evidence for tin nuclei in both the b.c.c. phase (1.4 mm/s absorption) and in nanograins of tin (absorption near 2.6 mm/s). The Mössbauer results give further confirmation for the structural picture given in Figs. 7 and 11.

Figs. 15 and 16 show that the center shift of the right hand absorption shifts to higher center shifts as the tin content increases. The spectra were fitted with a pair of Lorentzian singlets labeled 1 and 2 for the 2.6- and 1.4-mm/s absorptions, respectively. The fitting program varied the center position, the halfwidth and the intensity of each peak. The center shift of peak 1 and the fraction

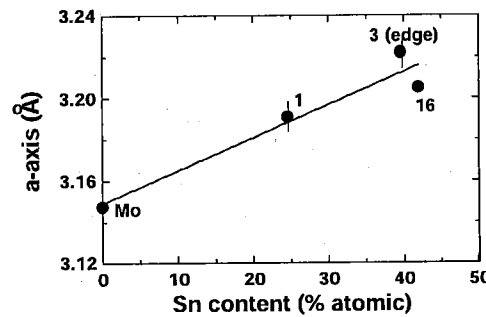


Fig. 14. Variation of the cubic lattice constant of the b.c.c. $\text{Mo}_{1-x}\text{Sn}_x$ phase vs. x . The sample numbers corresponding to the data points have been indicated.

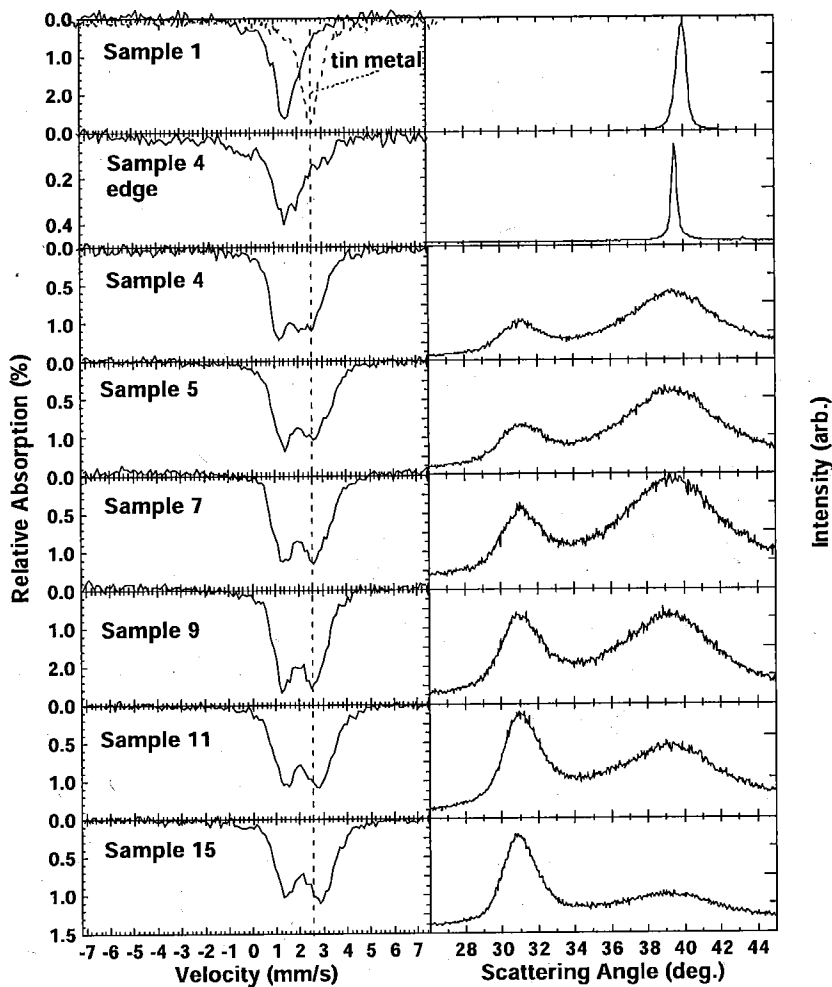


Fig. 15. Mössbauer spectra and X-ray patterns for thick/thick samples as indicated. The Mössbauer spectrum for tin metal is the dashed spectrum in the top left panel. The edge of sample 4 is also shown—this is a thin/thin sample.

of the total absorption found in peak 1 are given in Table 1. Fig. 17 shows the center shift of peak 1 vs. the percentage of tin in the samples.

The results for the intensity and center shift are difficult to understand. One would expect as the tin content increased and the number and size of the tin nanograins increased that the fraction of the Mössbauer intensity in peak one would increase. Table 1 shows that when the ‘tin’ absorption is present in thick/thick samples and in thin/thin samples with more than 42% tin, it always accounts for approximately 60% of the absorption intensity. A possible explanation for this ‘anomaly’ is that the recoil-free fraction of absorptions in the tin phase may decrease as the size and number of the tin regions increases. It is well known that bulk metallic tin has a small recoil-free fraction due to its low Debye temperature [16]. Thus, even though there is more tin phase present in samples with more tin, the fractional contribution of the tin phase to the spectrum

remains about the same due to the reduction in recoil-free fraction. In addition, as the number and size of the tin nanograins increases, we expect the center shift of the ‘tin’ peak to move toward that of tin (2.6 mm/s). However, Fig. 17 shows that there is not an asymptotic approach toward 2.6 mm/s as the tin content increases. We do not understand the reasons for the behavior in Fig. 17, and it will be the subject of future work.

It was hoped that by measuring the intensity of the endotherm associated with the melting of the tin grains that the amount of the tin phase in the samples could be quantified using differential scanning calorimetry (DSC) experiments. Fig. 18 shows DSC traces (measured in inert gas) for several samples between room temperature and 250 °C. The right side of Fig. 18 shows X-ray diffraction (XRD) patterns taken before and after the DSC scans for the corresponding samples. Sample 1, which is pure b.c.c. phase, shows no evidence for any phase transition and the X-ray diffraction pattern is

stable. Therefore the pure b.c.c. phase is stable to at least 250 °C. Heating substantially above 250 °C caused reactions between the tin in the samples and the copper substrate. Thick/thick samples 8 and 13 show exotherms with onsets near 120 °C and a corresponding dramatic change in the diffraction profile. The strength of the exotherm increases with the tin content. For both samples, the Bragg peak attributed to nanograins of tin (at 31°) is eliminated and a new peak appears near 33.3°. The peak corresponding to the b.c.c. phase (near 39.5°) of sample 13 also changes dramatically upon heating. The diffraction pattern of samples heated only to 150 °C is identical to these. This explains why there is no evidence for the melting of tin. By the time the samples reach the tin melting point (232 °C) there is no tin phase left! We do not yet understand the reaction corresponding to the exotherm, or the identity of the new phase which forms. Perhaps the new phase is MoSn_2 as reported in the provisional Mo–Sn phase diagram [10,11].

The bottom panel of Fig. 18 shows the DSC trace for thin/thin sample 19 and the XRD patterns before and after heating. For the thin/thin, sample the onset of the exotherm is at approximately 170 °C and is much broader than that observed for the thick/thick samples. The changes to the diffraction pattern are less obvious, but there is a clear shift of the shoulder near 31° in the unheated film to higher angle in the heated film. The peak corresponding to the b.c.c. phase also shifts to higher angle. Thus, there are some differences between the thermal behavior of the thick/thick and thin/thin films.

Finally, we have attempted to collect this structural information together in a structure–composition–temperature diagram shown in Fig. 19. We hesitate to call

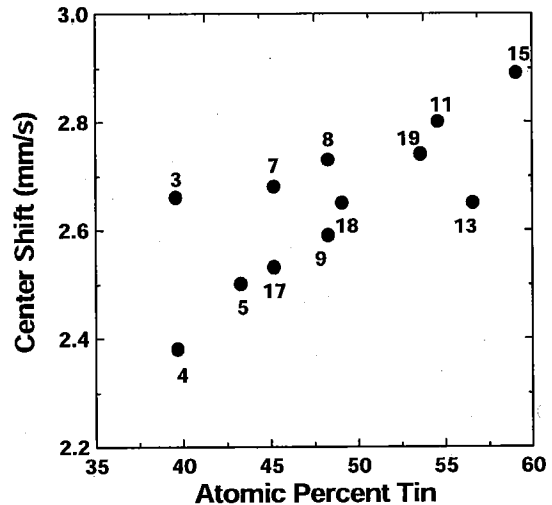


Fig. 17. The center shift of the absorption to the 'tin phase' plotted vs. overall tin content in the samples. The sample number corresponding to each data point has been plotted next to each point.

this a phase diagram since it describes the structures of metastable films. The italicized entries and solid lines are for the thin/thin films. The normal text entries and dashed lines are for the thick/thick films. The temperatures at which the sample points have been placed are simply to avoid clutter, and have no meaning.

4. Conclusion

Mo–Sn films made by sequential sputtering have been carefully characterized. In no case was a long-range artificial metallic superlattice formed. Instead, three main types of microstructure were observed: (1)

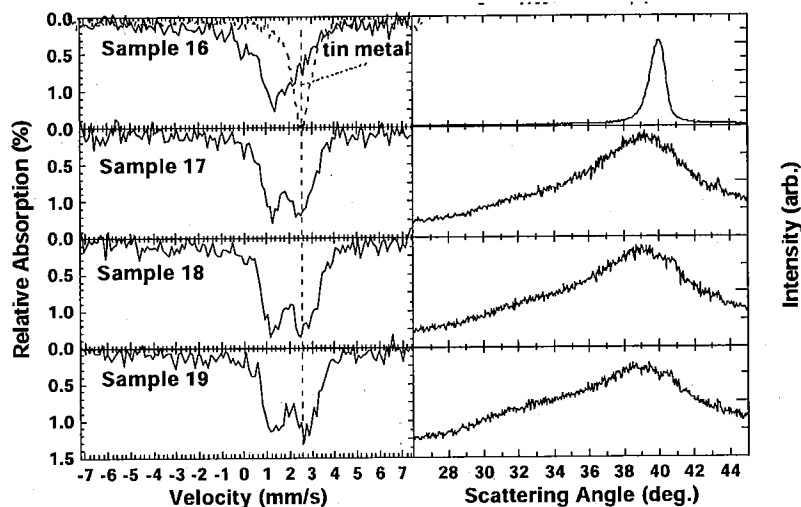


Fig. 16. Mössbauer spectra and X-ray patterns for thin/thin samples as indicated. The Mössbauer spectrum for tin metal is the dashed spectrum in the top left panel.

homogeneous crystalline body centered cubic $\text{Mo}_{1-x}\text{Sn}_x$ is produced when x is less than approximately 0.45 and when the layer thickness deposited in each pass under the targets is small; (2) nanocrystalline BCC $\text{Mo}_{1-x}\text{Sn}_x$ having x approximately equal to 0.45 coexisting with nanocrystalline tin when the overall tin content is greater than 45% atomic and the layer thickness deposited in each pass under the targets is small; and (3) lamina of composition modulated $\text{Mo}_{1-x}\text{Sn}_x$ disturbed by nanoscopic clusters of tin when the overall tin content is greater than approximately 40 at.% and the layer thickness of Mo deposited in each pass is greater than approximately 6 Å. This the first report of BCC $\text{Mo}_{1-x}\text{Sn}_x$ for $0 \leq x \leq 0.45$. The inability to prepare superlattices probably stems from the high surface diffusion rates of tin parallel to the surface.

The microstructure shown in Figs. 7 and 11 appear to be quite attractive as active/inactive alloy nanocomposites for anodes of Li-ion batteries. The electrochemical behavior of these materials is discussed in Turner et al. [14,17].

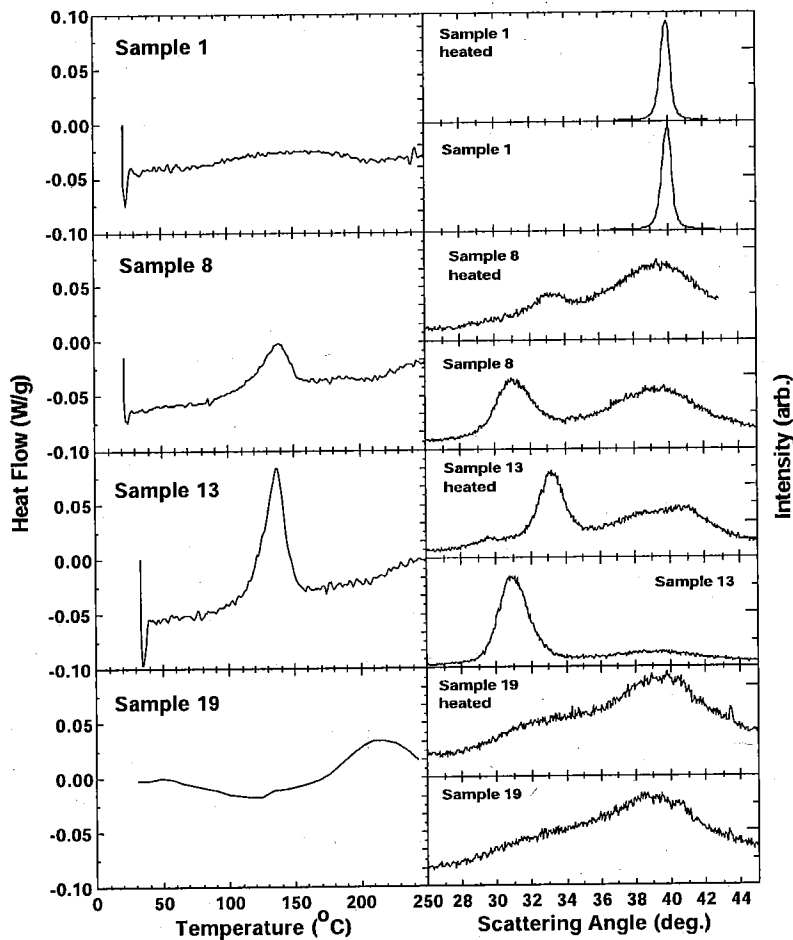


Fig. 18. DSC traces (left column) for samples as indicated. The right column shows the diffraction patterns before and after heating for the same samples as indicated.

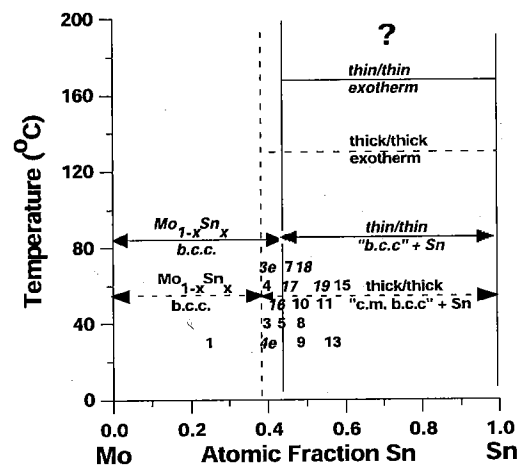


Fig. 19. Structure–composition–temperature diagram for the Mo–Sn films. The italicized points and the solid lines pertain to thin/thin samples and the normal font points and dashed lines to the thick/thick samples. The question mark indicates that the new phase that appears above the DSC exotherm is not understood.

There still remain several unanswered questions regarding these films. For example: what is the nature of the phase transformation in the thick/thick films at approximately 120 °C and in the thin/thin films at approximately 170 °C? Why does the Mössbauer center shift of the ‘tin phase’ approach values greater than 2.6 mm/s when the tin content of these samples gets large? Why does the intensity of the absorption due to the ‘tin phase’ always account for approximately 60% of the absorption when the tin nanograins are present? Mössbauer spectra collected at low temperature will help to answer the latter two questions and this will be one focus of our future work. A complete set of $\text{Mo}_{1-x}\text{Sn}_x$ film samples with $0.3 < x < 0.9$ would also be useful.

Acknowledgments

Part of this work was supported by NSERC and 3M Canada Co. under the Industrial Research Chair program.

References

- [1] L. Eckertova, Physics of Thin Films, Plenum Press, New York, 1986.

- [2] R. Clarke, F.J. Lamelas, S. Elagoz, in: R.F.C. Farrow, B. Dieny, M. Donath, A. Fert, B.D. Hermsmeier (Eds.), *Magnetism and Structure in Systems of Reduced Dimension*, Plenum Press, New York, 1993.
- [3] K.L. Chopra, *Thin Film Phenomena*, McGraw-Hill, New York, 1969.
- [4] B.Y. Jin, J.B. Ketterson, *Advances in Physics* 38 (1989) 189–366.
- [5] B.A. Boukamp, G.C. Lesh, R.A. Huggins, *J. Electrochem. Soc.* 128 (1981) 725.
- [6] R.A. Huggins, B.A. Boukamp, US Patent #4,436,796 (1984).
- [7] J. Yang, M. Winter, J.O. Besenhard, *Solid State Ionics* 90 (1996) 281.
- [8] O. Mao, J.R. Dahn, *J. Electrochem. Soc.* 146 (1999) 423.
- [9] O. Mao, B.L. Turner, D.W. McClure, I.A. Courtney, L.J. Krause, J.R. Dahn, *Electrochem. Soc. Lett.* 2 (1999) 3.
- [10] W.G. Moffat, *Handbook of Binary Phase Diagrams*, Genium Publishing Co, Schenectady, NY, 1990.
- [11] L.H. Brewer, *Bull. Alloy Phase Diagrams* 1 (1980) 40.
- [12] A. Brown, *Nature* 206 (1965) 502.
- [13] D.H. Killpatrick, *J. Phys Chem. Solids* 25 (1965) 1499.
- [14] R.L. Turner, D.J. McClure, L.J. Krause, M.I. Bucket, J.R. Dahn, O. Mao, Patent Cooperative Treaty Application WO 99/49532, 30 Sept. 1999.
- [15] B.E. Warren, *X-Ray Diffraction*, Addison-Wesley, Reading, Mass, 1969.
- [16] N.N. Greenwood, T.C. Gibb, *Mössbauer Spectroscopy*, Chapman and Hall Ltd, London, 1971.
- [17] R.L. Turner, L. Christensen, M.M. Bucket, J.R. Dahn, L.J. Krause, submitted to *Electrochemical and Solid State Letters*.